International Journal of Engineering Science 203 (2024) 104119

Contents lists available at ScienceDirect

International Journal of Engineering Science

journal homepage: www.elsevier.com/locate/ijengsci

Full length article

Multiphase thermo-hydro-mechanical coupled soil drying model with phase-exchange based on mixture coupling theory

Andrea Sendula [a], Kai Wang [b,c,d], Shashank B. Subramanyam [b,*], Jake Cray [a], Matthew Oram [a], Xiaohui Chen [b], Ana Heitor [b], David Harbottle [e], Kenny Brown [f]

[a] Centre for Doctoral Training in Fluid Dynamics, University of Leeds, Leeds LS2 9JT, UK
[b] School of Civil Engineering, University of Leeds, Leeds LS2 9JT, UK
[c] School of Earth and Environment, Anhui University of Science and Technology, Huainan, 232001, China
[d] College of Water Sciences, Beijing Normal University, Beijing, 100875, China
[e] School of Chemical Engineering, University of Leeds, Leeds LS2 9JT, UK
[f] N2–Applied AS, Askerveien 61, 1384 Asker, Norway

ARTICLE INFO

Keywords:
Mixture coupling theory
THM model
Multiphase
Soil drying

ABSTRACT

The drying phenomenon in soils involves complex interactions between thermal, hydrological, and mechanical effects within a multiphase system. While several researches (both mechanics and mixture theory approach) has been applied to study various thermo-hydro-mechanical (THM) coupled processes in porous media, incorporating both multiphase flow and phase change in soil drying remains limited. This work addresses this research gap by deriving new governing equations for a two-phase flow model suitable for soil drying by extending the mixture coupling approach. The derived model is implemented in COMSOL Multiphysics and validated against experimental data, demonstrating good agreement between the model predictions and the ob- served results. A sensitivity analysis is performed to investigate the impact of critical parameters on the drying process. The findings reveal that volumetric strain is most sensitive to Young's modulus, while the saturation of liquid water is most affected by intrinsic permeability. Additionally, preliminary results for a kaolinite clay sample during the drying process are presented, extending the applicability of the derived model to specific soil types. This research provides a comprehensive framework for fully THM coupled modelling of soil drying, which can serve as a basis for future investigations.

1. Introduction

The process of drying and evaporation of soil from the shallow subsurface describes a number of geotechnical and agricultural problems, from moisture content in soil impacting crop yields (Brutsaert & Chen, 1995; Erich & Hoskins, 2011; Ventura et al., 2001; Whalley et al., 2006; Whitmore & Whalley, 2009) to detection of buried objects and flows through landfills (Khalili & Loret, 2001; Simunek et al., 2001). However, a comprehensive model requires two-phase flow, phase changes, mechanical deformation, and thermal effects, resulting in a highly coupled system that is difficult to formulate.

Typically, the problem of soil drying is represented through simplified models, such as the soil water characteristic curve (SWCC), which describes the relationship between water content and matric suction. A common SWCC model used is suggested by van Genuchten (1980), but other models are presented by, for example, Brooks and Corey (1966) and Gardner (1970). It has also been

* Corresponding author.
E-mail address: S.B.Subramanyam@leeds.ac.uk (S.B. Subramanyam).

https://doi.org/10.1016/j.ijengsci.2024.104119
Received 28 March 2024; Received in revised form 9 June 2024; Accepted 11 July 2024
Available online 3 August 2024

shown that the SWCC can have a significant dependence on temperature changes (Bai et al., 2020), although this is often not necessary when temperature changes are small during convective drying (Tamizdoust & Ghasemi-Fare, 2022).

While these models offer valuable insights, they are limited in their description. The complete process of soil drying combines thermal, hydrodynamic, and mechanical (THM) effects, which impact, and are impacted by, each other. For example, soil shrinkage is known to occur during drying, especially in fine-grained soils (Dong et al., 2020). A more comprehensive model is required to obtain a complete picture of soil drying.

Few numerical models have attempted to capture convective drying within a fully coupled THM framework (Tamizdoust & Ghasemi-Fare, 2022), however, this a relatively new area of study, with more investigation needed (Lekshmi & Arnepalli, 2017). These models adopt a traditional mechanics approach, established by Terzaghi (1943) and extended by Biot (1941), which extends the stress–strain balance equations to capture the full model. However, this approach lacks a systematic coupling between each phase, hence is limited by the understanding of the coupling between the different phases, and the parameters involved in this coupling.

Another approach that has been used for THM models is mixture theory, (Rajagopal, 2010; Rajagopal & Saccomandi, 2016; Truesdell, 1957; Truesdell & Toupin, 1960), which is based on nonequilibrium thermodynamics. This approach uses energy and entropy balance for more precise constitutive equations. However, it fails to capture coupling in a realistic way, often describing the interactions between phases in a way that is hard to quantify experimentally for validation. This makes it unsuitable for complex coupled systems, such as evaporation of moisture from soil.

In recent years, non-equilibrium thermodynamics theory has been widely used in modelling the THM process, including works considering granular rearrangement (Bai et al., 2021, 2023) and bounded water (Zhang & Cheng, 2017), among others. However, the new approach, mixture coupling theory, based on non-equilibrium thermodynamics and mixture theory, does not require a detailed understanding of interaction between phases but develops the coupling from an entropy production perspective. This theory has shown a number of marked improvements when developing more complex THM models (Abdullah et al., 2022; Chen & Hicks, 2013; Chen et al., 2018; Jiao et al., 2022; Ma et al., 2022; Wang et al., 2022). In particular, it allows for the addition of new components without the need for strong physical assumptions of the mechanisms involved.

A number of steps have been made with mixture coupling theory that suggest its suitability for modelling soil drying. Wang et al. (2022) demonstrate how mixture coupling theory can be used with dynamic porosity, which is important for soil drying during which pore structure can change. Abdullah et al. (2022) model a two-phase flow, with water and gas present in the soil. Phase change between materials has been implemented through mixture coupling theory by Jiao et al. (2022). However, no attempt has been made to use mixture coupling theory to model soil drying, which requires phase change from liquid water to water vapour, dynamic porosity, and two-phase flow.

In this work, a new model is presented based on mixture coupling theory. This model incorporates thermal effects, mechanical and porous deformations, as well as two-phase flow and phase change, that capture the full dynamics of convective shallow subsurface soil drying.

In particular, the model developed will focus on capturing laboratory experiments of kaolinite clay drying under room temperature. This will allow for a number of simplifications to the full model that allow for easy comparison to experimental work.

2. Theory

2.1. Definitions

The following definitions are developed from the framework by Chen and Hicks (2013).

The mass flux of liquid water and water vapour is defined as

$$\mathbf{I}_l = \rho_l(\mathbf{v}_l - \mathbf{v}_s), \mathbf{I}_v = \rho_v(\mathbf{v}_v - \mathbf{v}_s) \tag{1}$$

where the superscripts $\alpha = l, v, s$ denote liquid water, water vapour and solid, respectively. ρ_α is the mixture density of each phase and $\mathbf{v}_\alpha$ the velocity of each phase. ρ_l and ρ_v are related to the true mass density through

$$\rho_l = \phi_l \rho_l^t, \rho_v = \phi_v \rho_v^t \tag{2}$$

where ρ_α^t represents the true mass density of each phase and ϕ^α is the volume fraction of each phase.

$$\phi = \phi_l + \phi_v \tag{3}$$

is the total porosity and

$$S_l = \frac{\phi_l}{\phi}, S_v = \frac{\phi_v}{\phi} \tag{4}$$

are the saturation of liquid water and water vapour.

2.2. Mass balance equations

For an arbitrary domain V with boundary Γ, the mass balance law for the αth phase is given by

$$\frac{D}{Dt}\int_V \rho_\alpha \, dV = \int_\Gamma \rho_\alpha(\mathbf{v}_\alpha - \mathbf{v}_s)\cdot \mathbf{n} \, d\Gamma + Q \tag{5}$$

where $\mathbf{n}$ is the unit outward normal, Q is a source term (representing phase change, for example) and the time derivative is defined as

$$\frac{D}{Dt} = \partial_t + \mathbf{v}_s \cdot \nabla \tag{6}$$

Using the divergence theorem, local equations can be found for the mass balance of each phase.

2.2.1. Liquid water

The mass balance equation for the liquid water is given by

$$\dot{\rho}_l + \rho_l \nabla \cdot \mathbf{v}_s + \nabla \cdot \mathbf{I}_l + \rho_l j_{lv} = 0 \tag{7}$$

where j_{lv} is the rate of moisture transport from liquid water to water vapour. Here, positive j_{lv} represents condensation and negative represents evaporation.

According to Darcy's law, the relative apparent velocity of the liquid water is

$$\mathbf{u}_l = -\frac{k_{rl}}{\eta_l} \kappa \nabla p_l \tag{8}$$

Here, k_{rl} is the relative permeability of liquid water, κ is the intrinsic permeability of the soil, p_l is the pressure of liquid water, and η_l is the dynamic viscosity of liquid water.

For the current focus of two-phase flow with phase change, the standard expression for Darcy's law can be used. However, mixture coupling theory does allow for this law to be extended to include the impact of thermal osmosis and water vapour pressure on the liquid water velocity, which may be useful for more detailed models, as demonstrated by Chen et al. (2009).

2.2.2. Water vapour

The mass balance equation for the water vapour is given by

$$\dot{\rho}_v + \rho_v \nabla \cdot \mathbf{v}_s + \nabla \cdot \mathbf{I}_v - \rho_l j_{lv} = 0 \tag{9}$$

As with liquid water, Darcy's law gives the relative apparent velocity of water vapour:

$$\mathbf{u}_v = -\frac{k_{rv}}{\eta_v} \kappa \nabla p_v \tag{10}$$

Here, k_{rv} is the relative permeability of water vapour, p_v is the pressure of water vapour, and η_v is the dynamic viscosity of water vapour.

2.3. Energy balance equations

2.3.1. Internal energy balance

The balance equation for internal energy is

$$\frac{D}{Dt} \int_V \epsilon \, dV = \int_\Gamma (\boldsymbol{\sigma} \mathbf{v}_s - \mathbf{I}'_q) \cdot \mathbf{n} \, d\Gamma - \int_\Gamma (h_l \mathbf{I}_l + h_v \mathbf{I}_v) \cdot \mathbf{n} \, d\Gamma \tag{11}$$

where h_α is the enthalpy density associated with enthalpy in phase $\alpha = l, v$. $\mathbf{I}'_q$ is the reduced heat flow associated with the conduction, while $h_\alpha \mathbf{I}_\alpha$ for $\alpha = l, v$ is associated with the convection in the liquid water and water vapour, respectively.

Using the divergence theorem, the local form of Eq. (11) can be written as

$$\dot{\epsilon} + \epsilon \nabla \cdot \mathbf{v}_s = \nabla \cdot \boldsymbol{\sigma} \mathbf{v}_s - \nabla \cdot \mathbf{I}'_q - h_l \nabla \cdot \mathbf{I}_l - h_v \nabla \cdot \mathbf{I}_v \tag{12}$$

2.3.2. Entropy balance

The entropy balance equation is

$$\frac{D}{Dt} \int_V \eta \, dV = \int_\Gamma -\mathbf{I}_\eta \cdot \mathbf{n} \, d\Gamma + \int_V \gamma \, dV \tag{13}$$

where the terms on the right describe entropy exchange and entropy production, respectively. The local version of Eq. (13) is

$$\dot{\eta} + \eta \nabla \cdot \mathbf{v}_s = -\nabla \mathbf{I}_\eta + \gamma \tag{14}$$

where $\mathbf{I}_\eta$ is the entropy flow, described as

$$\mathbf{I}_\eta = \frac{\mathbf{I}_q - \mu_l \mathbf{I}_l - \mu_v \mathbf{I}_v}{T} = \frac{\mathbf{I}'_q + T \eta_l^e \mathbf{I}_l + T \eta_v^e \mathbf{I}_v}{T} \tag{15}$$

Here, μ_α represents the chemical potential of each phase and η_α^e the entropy density.

2.3.3. Helmholtz free energy density balance

Helmholtz free energy density ψ is defined as $\psi = \epsilon - T\eta$, hence

$$\frac{D}{Dt}\int_V \psi\, dV = \frac{D}{Dt}\int_V \epsilon\, dV - \frac{D}{Dt}\int_V T\eta\, dV \tag{16}$$

Substituting Eq. (14) into the local form of Eq. (16) gives

$$\dot{\psi} + \psi\nabla\cdot\mathbf{v}_s - (\dot{\epsilon} + \epsilon\nabla\cdot\mathbf{v}_s) + \dot{T}\eta - T\nabla\cdot\mathbf{I}_\eta = -T\gamma \le 0 \tag{17}$$

The entropy production can be written as

$$T\gamma = -\mathbf{I}_\eta\cdot\nabla T - \mathbf{I}_l\cdot\nabla\mu_l - \mathbf{I}_v\cdot\nabla\mu_v \tag{18}$$

The first term on the right-hand side represents the thermal dissipative process associated with heat flux, while the other two featuring the divergence of the chemical potentials are the entropy production associated with the friction between the fluid and solid. This makes the assumption that the only sources of entropy are associated with thermal dissipation and friction at the fluid/solid boundaries. Any other entropy production, such as in phase change, has not been considered for this model.

We can then substitute Eqs. (12), (15) and (18) into Eq. (17) to obtain the Helmholtz free energy density balance equation:

$$\dot{\psi} + \psi\nabla\cdot\mathbf{v}_s = \nabla\cdot\boldsymbol{\sigma}\mathbf{v}_s - \nabla\cdot\mathbf{I}_q - \dot{T}\eta - \mu_l\nabla\cdot\mathbf{I}_l - \mu_v\nabla\cdot\mathbf{I}_v \tag{19}$$

2.3.4. Reference configuration

To find the equation for free energy density in the reference configuration, we start with classical continuum mechanics equations

$$\mathbf{F} = \frac{\partial\mathbf{x}}{\partial\mathbf{X}}(\mathbf{X},t), \mathbf{E} = \frac{1}{2}(\mathbf{F}^T\mathbf{F} - 1), J = \frac{dV}{dV_0}, \dot{J} = J\nabla\cdot\mathbf{v}_s \tag{20}$$

where $\mathbf{X}$ is an arbitrary reference configuration, $\mathbf{x}$ is the position at time t, $\mathbf{F}$ is the deformation gradient, $\mathbf{E}$ is Green strain, J is the determinant of the deformation gradient, dV is the volume of the current configuration and dV_0 is the volume of the reference configuration.

The equation for free energy density at the reference configuration can be found by multiplying Eq. (19) by J,

$$\dot{\Psi} = tr(\mathbf{T}\dot{\mathbf{E}}) - \dot{T}J\eta - J\mu_l\nabla\cdot\mathbf{I}_l - J\mu_v\nabla\cdot\mathbf{I}_v \tag{21}$$

where $\Psi = J\psi$ is the free energy density at the reference configuration and $\mathbf{T}$ is the second Piola–Kirchhoff stress.

From Eqs. (7) and (9), Eq. (21) becomes

$$\dot{\Psi} = tr(\mathbf{T}\dot{\mathbf{E}}) - \dot{T}J\eta + \mu_l\dot{m}_l + \mu_v\dot{m}_v \tag{22}$$

where $m_\alpha = J\rho_\alpha$ is the mass density of each pore phase in the reference configuration.

2.3.5. Helmholtz free energy density of the pore water (liquid/gas)

The free energy density of a mixture of liquid water and water vapour in a pore can be written using classical thermodynamics,

$$\psi_{pore} = -\bar{p} + S_l\rho_l^t\mu_l + S_v\rho_v^t\mu_v \tag{23}$$

where the pressure in the pores is approximated as the average pressure, $\bar{p} = p_lS_l + p_vS_v$.

The Gibbs-Duhem equation provides

$$\dot{\bar{p}} - \dot{T}S_l\eta_l - \dot{T}S_v\eta_v = S_l\rho_l^t\dot{\mu}_l + S_v\rho_v^t\dot{\mu}_v \tag{24}$$

which can be substituted into Eq. (23) to obtain

$$\dot{\psi}_{pore} = -\dot{T}S_l\eta_l - \dot{T}S_v\eta_v + \mu_l(S_l\rho_l^t)^{\cdot} + \mu_v(S_v\rho_v^t)^{\cdot} \tag{25}$$

2.3.6. Helmholtz free energy density of the wetted soil matrix

The free energy density of the wetted soil matrix can be found by subtracting the free energy of the pore water from the total free energy. This leads to

$$(\Psi - J\phi\psi_{pore})^{\cdot} = tr(\mathbf{T}\dot{\mathbf{E}}) + \dot{v}\bar{p} - \dot{T}H_s \tag{26}$$

where $v = J\phi$ is the pore volume per unit reference volume and $H_s = J\eta_s$ is the reference entropy density of the solid.

The deformation potential density is defined as

$$W = (\Psi - J\phi\psi_{pore}) - v\bar{p} \tag{27}$$

hence its time derivative becomes

$$\dot{W} = tr(\mathbf{T}\dot{\mathbf{E}}) - \dot{T}H_s - v\dot{\bar{p}} \tag{28}$$

Eq. (28) implies W is a function of $\mathbf{E}, \bar{p}$ and T, so the following equations can be obtained:

$$T_{ij} = \left(\frac{\partial W}{\partial E_{ij}}\right)_{\bar{p},T}, \upsilon = -\left(\frac{\partial W}{\partial \bar{p}}\right)_{E_{ij},T}, H_s = -\left(\frac{\partial W}{\partial T}\right)_{\bar{p},E_{ij}} \tag{29}$$

Therefore, substituting Eqs. (29) into (28) gives

$$\dot{W}(\mathbf{E}, \bar{p}, T) = \left(\frac{\partial W}{\partial E_{ij}}\right)_{\bar{p},T} \dot{E}_i j + \left(\frac{\partial W}{\partial \bar{p}}\right)_{E_{ij},T} \dot{\bar{p}} + \left(\frac{\partial W}{\partial T}\right)_{\bar{p},E_{ij}} \dot{T} \tag{30}$$

We also obtain the following set of equations

$$\dot{T}_{ij} = L_{ijkl}\dot{E}_{kl} - M_{ij}\dot{\bar{p}} + S^q_{ij}\dot{T} \tag{31}$$

$$\dot{\upsilon} = M_{ij}\dot{E}_{ij} + Q\dot{\bar{p}} + B_q\dot{T} \tag{32}$$

$$\dot{H}_s = -S^q_{ij}E_{ij} + B_q\dot{\bar{p}} + Z_q\dot{T} \tag{33}$$

where $L_{ijkl}, M_{ij}, S^q_{ij}, Z_q, B_q, Q$ are material-dependent constants defined as follows:

$$L_{ijkl} = \left(\frac{\partial T_{ij}}{\partial E_{kl}}\right)_{\bar{p},T} = \left(\frac{\partial T_{kl}}{\partial E_{ij}}\right)_{\bar{p},T} \tag{34}$$

$$M_{ij} = -\left(\frac{\partial T_{ij}}{\partial \bar{p}}\right)_{E_{ij},T} = \left(\frac{\partial \upsilon}{\partial E_{ij}}\right)_{\bar{p},T} \tag{35}$$

$$S^q_{ij} = -\left(\frac{\partial T_{ij}}{\partial T}\right)_{E_{ij},\bar{p}} = -\left(\frac{\partial H_s}{\partial E_{ij}}\right)_{\bar{p},T} \tag{36}$$

$$Z_q = \left(\frac{\partial H_s}{\partial T}\right)_{E_{ij},\bar{p}} \tag{37}$$

$$B_q = \left(\frac{\partial \upsilon}{\partial T}\right)_{E_{ij},\bar{p}} = \left(\frac{\partial H_s}{\partial \bar{p}}\right)_{E_{ij},T} \tag{38}$$

$$Q = \left(\frac{\partial \upsilon}{\partial \bar{p}}\right)_{E_{ij},T} \tag{39}$$

For this derivation, we ignore the changes in H_s and focus on variations of T_{ij} and υ with respect to time.

2.4. Governing equations

The following assumptions are made to simplify the equations:

- The mechanical behaviour can be considered as a small strain condition, so the Green strain tensor E_{ij} and the Piola–Kirchhoff stress T_{ij} can be replaced with the strain tensor ϵ_{ij} and the Cauchy stress σ_{ij}.
- The porous media is assumed to be isotropic to avoid mathematical complexity.
- The parameters $L_{ijkl}, M_{ij}, S^q_{ij}, Z_q, B_q, Q$ are material-dependent constants, so must also be isotropic.

Using the fact that the material-dependent constants are isotropic, the tensors M_{ij} and S^q_{ij} are diagonal and can be written as

$$M_{ij} = \zeta\delta_{ij}, S_{ij} = \omega_T\delta_{ij} \tag{40}$$

where ζ is Biot's coefficient and ω_T is the thermal expansion coefficient of the soil.

The elastic stiffness L_{ijkl} can be written as a fourth-order isotropic tensor,

$$L_{ijkl} = G(\delta_{ik}\delta_{jl} + \delta_{il}\delta_{jk}) + \left(K - \frac{2G}{3}\right)\delta_{ij}\delta_{kl} \tag{41}$$

where G is the shear modulus and K is the bulk modulus.

2.4.1. Mechanical equation

Using the previous assumptions and the isotropic expressions in Eqs. (40) and (41), Eq. (31) can be changed to the following form:

$$\dot{\sigma}_{ij} = \left(K - \frac{2G}{3}\right)\dot{\epsilon}_{kk}\delta_{ij} + 2G\dot{\epsilon}_{ij} - \zeta\dot{\bar{p}}\delta_{ij} + \omega_T\dot{T}\delta_{ij} \tag{42}$$

The time derivative of $\bar{p}$ can be written as

$$\dot{\bar{p}} = (S_l + C^p_s p_c)\dot{p}_l + (S_v - C^p_s p_c)\dot{p}_v \tag{43}$$

where $C^p_s = \frac{\partial S_l}{\partial p_c}$ is the specific moisture capacity and $p_c = p_g - p_w$ is the capillary pressure.

Then Eq. (42) can be rewritten as

$$\dot{\sigma}_{ij} = \left(K - \frac{2G}{3}\right)\dot{\epsilon}_{kk}\delta_{ij} + 2G\dot{\epsilon}_{ij} - \zeta(S_l + C_s p_c)\dot{p}_l\delta_{ij} - \zeta(S_v - C_s^p p_c)\dot{p}_v\delta_{ij} + \omega_T\dot{T}\delta_{ij} \tag{44}$$

The first two terms on the right hand side represent the elastic deformation of the solids, while the next two are the coupling terms associated with the liquid water and water vapour pressure from the pores. The final term is the temperature coupling term.

Assuming mechanical equilibrium $\frac{\partial\sigma_{ij}}{\partial x_j} = 0$ and using displacement variables $d_i (i = 1, 2, 3)$ through $\epsilon_{ij} = \frac{1}{2}(d_{i,j} + d_{j,i})$ leads to

$$G\nabla^2\dot{\mathbf{d}} + \left(\frac{G}{1-2\theta}\right)\nabla(\nabla\cdot\dot{\mathbf{d}}) - \zeta\nabla[(S_l + C_s^p p_c)\dot{p}_l] - \zeta\nabla[(S_v - C_s^p p_c)\dot{p}_v] + \nabla[\omega_T\dot{T}] = 0 \tag{45}$$

where θ is Poisson's ratio.

2.4.2. Porosity

Similarly to the mechanical equation, we obtain an equation for the pore fraction by applying our assumptions to Eq. (32):

$$\dot{\upsilon} = \zeta\dot{\epsilon}_{ii} + Q\dot{\bar{p}} + B_q\dot{T} \tag{46}$$

Rewriting $\bar{p}$ in term of the liquid water and water vapour pressures and ϵ_{ij} in terms of the displacement variables, the porosity equation becomes

$$\dot{\upsilon} = \zeta\nabla\cdot\dot{\mathbf{d}} + Q\left((S_l + C_s^p p_c)\dot{p}_l + (S_v - C_s^p p_c)\dot{p}_v\right) + B_q\dot{T} \tag{47}$$

2.4.3. Liquid water phase

Substituting the expressions for mass flux of liquid water from Eq. (1), liquid water density from Eq. (2), saturation from Eq. (4), the liquid water balance Eq. (7) becomes

$$(\rho_l^t\phi S_l)^{\cdot} + \rho_l^t\phi S_l\nabla\cdot\mathbf{v_s} + \nabla\cdot\left(\rho_l^t\phi\$_l(\mathbf{v}_l - \mathbf{v}_s)\right) + \rho_l^t\phi S_l j_{lv} = 0 \tag{48}$$

Then Darcy's velocity, Eq. (8), implies

$$(\rho_l^t\phi S_l)^{\cdot} + \rho_l^t\phi S_l\nabla\cdot\mathbf{v_s} + \nabla\cdot\left(\rho_l^t\mathbf{u}_l\right) + \rho_l^t\phi S_l j_{lv} = 0 \tag{49}$$

Multiplying through by the Jacobian J and using the previously defined identities, the liquid water balance equation can be written as

$$(S_l\upsilon\rho_l^t)^{\cdot} + \nabla\cdot(\rho_l^t\mathbf{u}_l) + \rho_l^t S_l\upsilon j_{lv} = 0 \tag{50}$$

Substituting Eq. (8) into the balance equation and rewriting $\epsilon_{ij}, \bar{p}$ using previous expressions, the full equation for the liquid water phase can be written as

$$S_l\dot{\upsilon} + \upsilon\dot{S}_l + \upsilon S_l\frac{\dot{p}_l}{K_l} - \nabla\cdot\left(\frac{k_{rl}}{\eta_l}\kappa\nabla p_l\right) + S_l\upsilon j_{lv} = 0 \tag{51}$$

Here, K_l is the bulk modulus of liquid water and the rate of change of water density is given by $\dot{\rho}_l^t = \rho_l^t\frac{\dot{p}_l}{K_l}$.

2.4.4. Water vapour phase

Similarly to the liquid water, we can obtain the following full equation for the water vapour phase:

$$S_v\dot{\upsilon} + \upsilon\dot{S}_v + \upsilon S_v\frac{\dot{p}_v}{K_v} - \nabla\cdot\left(\frac{k_{rv}}{\eta_l}\kappa\nabla p_v\right) - S_l\upsilon j_{lv}\frac{\rho_l^t}{\rho_v^t} = 0 \tag{52}$$

Here, K_v is the bulk modulus of water vapour.

2.4.5. Thermal equation

The balance equation for heat transport is given by

$$\frac{D}{Dt}\int_V (q_s + q_l + q_v)\,dV = -\int_\Gamma \mathbf{I}_q\cdot\mathbf{n}\,d\Gamma + Q \tag{53}$$

hence the local version can be written as

$$(q_s + q_l + q_v)^{\cdot} + (q_s + q_l + q_v)\nabla\cdot\mathbf{v}_s + \nabla\cdot\mathbf{I}_q - L\rho_l j_{lv} = 0. \tag{54}$$

Here, $q_\alpha = \rho_\alpha C_\alpha T$ is the heat density of each phase, where C_α is the specific heat capacity of each phase. Multiplying through by the Jacobian J transforms the equation into

$$(Jq_s + Jq_l + Jq_v)^{\cdot} + J\nabla\cdot\mathbf{I}_q - J\rho_l j_{lv} = 0 \tag{55}$$

and using thermo densities relative to the partial densities, $q_\alpha^\alpha = \frac{q_\alpha}{S_\alpha\phi}$,

$$(q_s^s(J-\upsilon) + \upsilon q_l^l S_l + \upsilon q_v^v S_v)^{\cdot} + J\nabla\cdot(\mathbf{I}_q' + h_l\mathbf{I}_l + h_v\mathbf{I}_v) - J\rho_l^t\phi S_l L j_{lv} = 0 \tag{56}$$

Substituting an expression for the reduced heat flux, $\mathbf{I}'_q = -\frac{L_l^q \rho_l^l}{p_l}\nabla p_l - \frac{L_v^q \rho_v^v}{p_v}\nabla p_v - \lambda \nabla T$, and using $\mathbf{I}_l = \mathbf{u}_l \rho_l^t, \mathbf{I}_v = \mathbf{u}_v \rho_v^t$, the balance equation for heat transport becomes

$$\begin{aligned}&(S_l \upsilon \rho_l^t C_l T + S_v \upsilon \rho_v^t C_v T + (1-\upsilon)\rho_s^t C_s T)^{\cdot} \\ &+J\nabla \cdot \left(-\frac{L_l^q \rho_l^t}{p_l}\nabla p_l - -\frac{L_v^q \rho_v^t}{p_v}\nabla p_v - \lambda \nabla T\right) \\ &+J\nabla \cdot \left(\rho_l^t \mathbf{u}_l C_l T + \rho_v^t \mathbf{u}_v C_v T\right) - \rho_l^t S_l \upsilon j_{lv} L = 0\end{aligned} \tag{57}$$

L is the latent heat of vaporisation of liquid water, while L_α^q are the pressure diffusion coefficients for thermal effects, for $\alpha = l, v$.

For this model, we ignore thermal coupling due to pressure, so the final equation used is

$$\begin{aligned}&(S_l \upsilon \rho_l^t C_l T + S_v \upsilon \rho_v^t C_v T + (1-\upsilon)\rho_s^t C_s T)^{\cdot} \\ &+\nabla \cdot (-\lambda \nabla T) + \nabla \cdot \left(\rho_l^t \mathbf{u}_l C_l T + \rho_v^t \mathbf{u}_v C_v T\right) - \rho_l^t S_l \upsilon j_{lv} L = 0\end{aligned} \tag{58}$$

Eqs. (46), (47), (51), (52), and (58) provide a closed system of five coupled equations to solve five variables, $\mathbf{d}, \upsilon, p_l, p_v$, and T and are used as the basis of the numerical model.

2.5. Key parameters

The quantity ζ is Biot's coefficient and is related to the bulk moduli K and K_s. Here, we assume that a poroelastic relationship holds and that K_s, the bulk modulus of the solid matrix, is very large. Hence,

$$\zeta = 1 - \frac{K}{K_s} \approx 1 \tag{59}$$

and the value $\zeta = 1$ will be used in the numerical simulations.

The void compressibility can be written using ζ as

$$Q = \frac{1}{K_s}(\zeta - \upsilon) + \frac{\upsilon S_l}{K_l} + \frac{\upsilon S_v}{K_v} \tag{60}$$

B_q, the coefficient for thermal-induced porosity changes, can be defined as

$$B_q = \frac{\upsilon - \zeta}{\omega_T K} \tag{61}$$

for thermal expansion coefficient ω_T.

The saturation of liquid water was defined using the van Genuchten model (van Genuchten, 1980),

$$S_l = \left(\left(\frac{p_c}{M}\right)^{\frac{1}{1-m}} + 1\right)^{-m} \tag{62}$$

and the saturation of water vapour is defined as $S_v = 1 - S_l$.

The relative permeability of liquid water and water vapour can also be defined using the van Genuchten parameters, m, M,

$$k_{rl} = \sqrt{S_l}\left(1 - \left(1 - S_l^{\frac{1}{m}}\right)^m\right)^2 \tag{63}$$

and $k_{rv} = 1 - k_{rl}$.

The phase change j_{lv} takes the non-equilibrium assumption where

$$j_{lv} \propto (\rho_v - \rho_{ve}), \tag{64}$$

for ρ_{ve}, the equilibrium water vapour density (Massman, 2015). This is defined using the Ostwald–Freundlich equation to model water activity,

$$\rho_{ve} = \rho_v^t e^{\frac{-M_w p_c}{R \rho_l^t T}} \tag{65}$$

with the molar mass of water vapour $M_w = 0.018$ g/mol and universal gas constant $R = 8.3145$ J/mol, following Massman (2015).

For simplicity, the proportionality coefficient (m_e) is assumed to be a constant, determined from experimental data. Therefore,

$$j_{lv} = m_e(\rho_v^t \upsilon S_v - \rho_{ve}) \tag{66}$$

where m_e is the phase change coefficient.

The latent heat of vaporisation is taken from Monteith and Unsworth (2013) and given by

$$L = 2.501 \times 10^6 - 2369.2(T + 273.15). \tag{67}$$

Table 1
Initial conditions in numerical simulation.

Displacement	0 m
Porosity	0.575
Liquid water pressure	0 Pa
Water vapour pressure	10^5 Pa
Temperature	293.15 K

2.6. Boundary conditions

The surface evaporation term is represented by

$$J_e = m_v(\rho_{ve} - \rho_v^t(RH)_a) \tag{68}$$

where m_v is the vapour flux coefficient, ρ_{ve} is the equilibrium water vapour density, and $(RH)_a$ is the relative humidity of the atmosphere. This follows the form suggested by Tamizdoust and Ghasemi-Fare (2022).

The thermal energy exchange across the top boundary is described by conductive heat flux as well the latent heat of evaporation, as done by Tamizdoust and Ghasemi-Fare (2022). In natural conditions or those where high temperatures are involved (Massman, 2015), infrared radiation, such as thermal solar energy, can also be important. However, within the controlled drying condition modelled here, this term can be neglected. Therefore, the boundary condition representing the thermal energy exchange can be written as

$$G = -m_h(T_{surf} - T_a) - LJ_e \tag{69}$$

where G is the heat flux. On the right hand side, the first term is the conductive heat flux, where m_h is the convective heat transfer coefficient, T_{surf} is the temperature at the surface of the soil, and T_a is the temperature of the atmosphere. T_a can vary in natural conditions, for example, due to diurnal or seasonal changes, but for this model, it was assumed to be constant. The second term is the latent heat of evaporation.

3. Numerical modelling

3.1. Numerical implementation

The governing equations (Eqs. (46), (47), (51), (52), and (58)) were solved using COMSOL Multiphysics v6.0. The numerical implementation was set up to represent the drying of a square sample of kaolinite clay, representative of laboratory experiments.

A 2D square domain was used to represent a cross-section of the soil sample. The domain was discretised using a rectangular mesh, with a boundary layer at the upper surface, with a total of 1656 elements after mesh sensitivity analysis. The grid convergence index was calculated based on saturation after a fixed time and gave a discretisation error of 0.0007%. The kaolinite clay was initially saturated and at room temperature. The initial values for each variable solved for were set as specified in Table 1. Thermal insulation and no mass flux conditions are imposed along the sides and base of the domain. Displacements perpendicular to the sides and base are also set at 0. No mass flux is imposed for the liquid water along the top boundary, while vapour flux and heat flux conditions as described before represent the exchanges with the atmosphere. A free boundary condition is set for the displacement along the top boundary. Fig. 1 summarises the initial conditions and boundary conditions.

A segregated solver was used to solve the five coupled equations in order to reduce the memory requirements. A relative tolerance of 0.001 was used. An implicit Backward Differentiation Formula (BDF) solver was used for the timestepping. The temperature used linear discretisation, while all other variables used quadratic discretisation.

3.2. Variable and parameter settings

Kaolinite is a well-packed mineral, with a 1:1 octahedral-tetrahedral layering structure, that gives it non-expanding properties (Miranda-Trevino & Coles, 2003). Many experiments have been conducted on both saturated and unsaturated kaolinite in order to understand its thermal, hydraulic, and mechanical properties. The data from these experiments has been used to set the variables and model settings for the results presented in this report, in accordance with the literature (Akin & Likos, 2020; Engineering ToolBox, 2004; Mondol et al., 2008; Vollet et al., 1994).

The values used in the COMSOL simulation can be found in Table 2. Any value not included was taken from the built-in material library in COMSOL for H20 (water) [gas] and H20 (water) [liquid] (Chase, 1998; Hammouda & Mihoubi, 2014; Mcbride et al., 1993; Pankratz, 1982; Weast, 1998).

The values selected have been chosen to be representative of those presented in the literature, however, there exists variation between kaolinite samples and the reported values. A sensitivity study has been conducted for key parameters, to determine the impact of parameter variability, which is discussed in the following section.

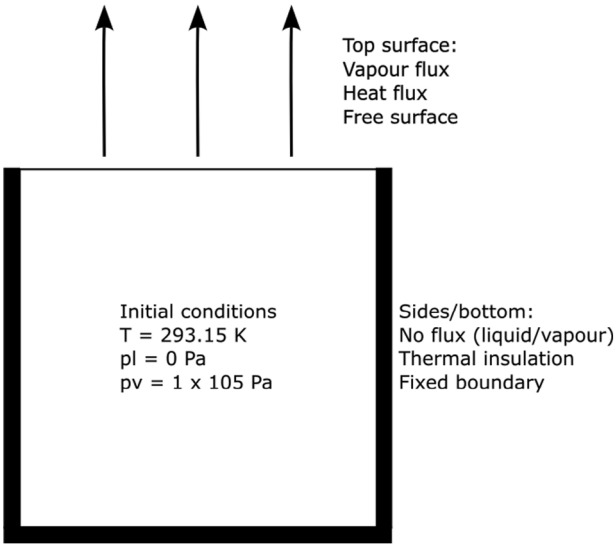

Fig. 1. Initial and boundary conditions used for computational modelling.

Table 2
Values used for numerical modelling.

C_s, specific heat capacity of kaolinite	945 J/kg K
C_v, specific heat of water vapour	1864 J/kg K
E, Young's modulus	1 MPa
K_l, bulk modulus of liquid water	2.18 GPa
K_s, bulk modulus of kaolinite	44 GPa
K_v, bulk modulus of water vapour	1 kPa
m, van Genuchten parameter	0.6
M, van Genuchten parameter	5.632×10^5 Pa
m_e, phase change coefficient	1×10^{-6} 1/s
m_h, convective heat transfer coefficient	10000 W/m^2 K
m_v, vapour flux coefficient	6×10^{-6} m/s
$(RH)_a$, relative humidity of atmosphere	50%
β_s, thermal expansion coefficient of solid	1.86×10^{-5}
ζ, Biot's coefficient	1
κ, intrinsic permeability	1×10^{-16}
λ, thermal conductivity	1.1
ν, Poisson ratio	0.36
ρ_s, density of kaolinite	2.86 g/cm^3

4. Validation of SWCC

The SWCC used in the model was validated through comparison to experimental results measuring gravimetric water content against the capillary pressure.

Soil samples were mixed with a water content 1.5LL = 97.5% and left for 48 h to homogenise. 5 ml samples, modelled using a 1 cm by 1 cm 2D model, were transferred into a plastic container provided with the WP4C Dewpoint Potentiameter. The initial mass of each slurry was recorded and they were left to air dry.

As the samples dried, they were routinely weighed and placed into the WP4C to determine the total suction. The WP4C was set to precise mode, which continuously takes readings until 3 consecutive measurements are within a threshold. At the end of drying, the samples were left for 24 h in a 100 °C oven to calculate the dry soil mass.

Once the samples finished the drying cycle, the weights were transformed to gravimetric water content through: $\theta = m_i/m_s$, where m_i is the ith weight and m_s is the mass of the soil. The experimental data from one sample was used to calibrate the model parameters, while data from all the samples was used for validation. The results from the soil drying test have been plotted in Fig. 2.

The parameters in Table 2 were calibrated to be representative of the experimental results. The initial conditions in Table 1 were representative of the experimental conditions.

The error between the numerical and experimental results was quantified using the root square mean error, the normalised root square mean error, the relative average error, and the correlation coefficient. These are defined as follows:

$$RSME = \sqrt{\sum_{i=1}^{n} \frac{(M_i - E_i)^2}{n}} \tag{70}$$

Table 3
Calculated errors between numerical model and experimental results.

Error estimation	Sample A	Sample B	All samples
RSME	0.0358	0.0285	0.0324
NRSME	0.0766	0.0604	0.0671
AVRE	1.0280	0.9643	0.9962
R	0.9814	0.9850	0.9827

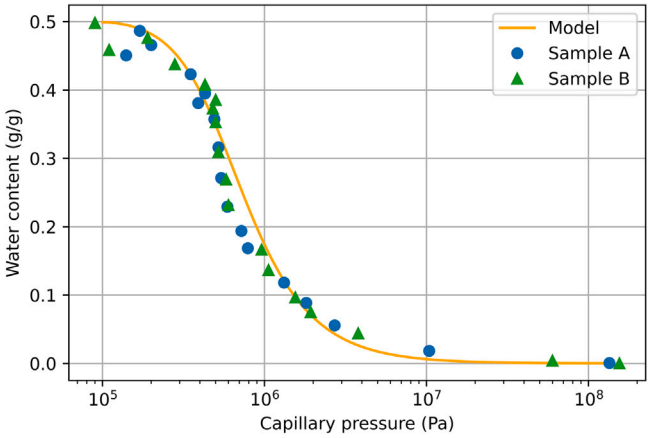

Fig. 2. Volumetric water content against capillary pressure, plotted for COMSOL results and experimental data.

$$NRSME = \frac{RSME}{E_{max} - E_{min}} \tag{71}$$

$$AVRE = \sum_{i=1}^{n} |\frac{M_i}{E_i}|/n \tag{72}$$

$$R = \frac{\sum_{i=1}^{n}(M_i - \bar{M})(E_i - \bar{E})}{\sqrt{\sum_{i=1}^{n}(M_i - \bar{M})^2 \sum_{i=1}^{n}(E_i - \bar{E})^2}} \tag{73}$$

Here, M_i represents the model values, E_i represents the experimental data, $\bar{M}$ and $\bar{E}$ are the averages of the model and experimental values respectively, and E_{max}, E_{min} are the maximum and minimum values of the experimental data.

The results of the numerical model were compared with the experimental data and the calculated errors were found between the numerical values and all experimental samples. A summary of the errors can be found in Table 3. A comparison of the water content against capillary pressure for the numerical model and the experimental samples can be found in Fig. 2.

As described in Table 3, the numerical data shows good similarity to the experimental results. The RSME and NRSME of each sample are both low. The AVRE is also fairly low, with the highest (Sample A), still demonstrating a fairly low relative average error. The correlation coefficient is larger than 0.95 for all the samples, showing a high correlation between the numerical and experimental results.

In Fig. 2, the full simulated curve and experimental values are plotted. As can be seen, there is a strong agreement between the shape of the curve and the experimental trend. The greatest errors are at around $p_c = 10^6$ Pa, about halfway through the drying process. However, the trends shown are still very similar.

It can be concluded that the numerical and experimental values show strong agreement, therefore the model and chosen variables are suitable for simulating soil drying and can provide accurate insights into the behaviour of the thermal, hydraulic, and mechanical behaviour of soil during the drying process. Further results will demonstrate other trends that match those in the literature.

5. Sensitivity analysis of computational model

5.1. Methodology

The sensitivity of the model to variations in parameters was assessed using the ratio of parameter variation (ROV) (Cheviron & Coquet, 2009). This method analyses variations in the parameters and results to determine the sensitivity to each parameter. The ROV is calculated using

$$ROV(t) = \frac{[c(t) - c_{ref}(t)]/|c_{ref}(t)|}{(p - p_{ref})/p_{ref}} \tag{74}$$

Table 4
Values used for sensitivity study.

Parameter	−60%	−30%	–	30%	60%
κ	4×10^{-17}	7×10^{-17}	1×10^{-16}	1.3×10^{-16}	1.6×10^{-16}
E [MPa]	0.4	0.7	1	1.3	1.6
m_v [m/s]	2.4×10^{-6}	4.2×10^{-6}	6×10^{-6}	7.8×10^{-6}	9.6×10^{-6}
$(RH)_a$	0.2	0.35	0.5	0.65	0.8
m_e [1/s]	4×10^{-7}	7×10^{-1}	1×10^{-6}	1.3×10^{-6}	1.6×10^{-6}

Table 5
Calculated ROV for each parameter for volumetric strain.

Parameter	Variation (%)	ROV_{min}	ROV_{max}	ROV_{ave}
κ	−60	−2.52	−0.939	−2.45
	−30	−1.44	−0.629	−1.40
	30	0.395	0.772	0.755
	60	0.336	0.627	0.613
E	−60	−2.52	−2.50	−2.51
	−30	−1.44	−1.43	−1.43
	30	0.769	0.771	0.770
	60	0.625	0.626	0.625
m_v	−60	−1.00	−0.806	−0.949
	−30	−0.994	−0.783	−0.906
	30	0.621	0.981	0.751
	60	0.477	0.980	0.573
$(RH)_a$	−60	−0.981	−0.478	−0.574
	−30	−0.982	−0.623	−0.757
	30	0.785	1.01	0.916
	60	0.807	1.02	0.960
m_e	−60	−1.22	−0.000238	−1.13
	−30	−0.792	−0.000238	−0.586
	30	0.0000700	0.574	0.255
	60	0.0000950	0.523	0.199

Here, $c_{ref}(t)$ is the calculated value of the reference model at a specified time, $c_{(t)}$ is the calculated value of the variation model at a specified time, p_{ref} is the parameter value of the reference model, and p is the parameter model of the variation model.

For each calculation for the sensitivity analysis, one parameter was selected to be varied while the others remained fixed. ROV was used to analyse the sensitivity to that parameter. The maximum, minimum, and average values for the ROV were found for each parameter to understand the sensitivity across the entire time of the simulation.

The parameters used for the sensitivity study are listed in Table 4. These are κ, the intrinsic permeability; E, Young's modulus of kaolinite; m_v, the rate of vapour evaporation into the atmosphere; $(RH)_a$, the relative humidity of the atmosphere; and m_e, the phase change coefficient. The variations are taken at 30% and 60% from the value used in the final simulations, with this range being based on previous studies for THM models (Selvadurai et al., 2019; Wang et al., 2022).

5.2. Sensitivity analysis results

The sensitivity analysis was conducted comparing results for volumetric strain and liquid saturation, to evaluate the sensitivity of the mechanical behaviour and hydraulic changes respectively.

5.2.1. Mechanical behaviour

The volumetric strain against time plotted for variation of parameters can be found in Figs. 3, 4, 5, 6 and 7, and the corresponding ROV can be found in Table 5. In almost all cases, we see the same trend, with the volumetric strain becoming more negative and gradually tending towards some fixed value, however, this value depends on the parameter variation. The greatest differences in results lie towards the final time of the simulation, however, there remains notable differences at all times.

However, for variations in the phase change coefficient, we see much greater differences between the shape of volumetric strain against time. For the smallest phase change coefficient, the strain changes only slightly with time, while with higher values, the strain drops much quicker. This demonstrates the importance of the selection of phase change coefficient.

The higher the absolute value of ROV, the more sensitive a parameter is to variation. For the tested values, volumetric strain is most sensitive to the material properties, permeability and Young's modulus, with these demonstrating some of the highest ROVs. However, these parameters are only approximately doubly as sensitive as m_v, $(RH)_a$ and m_e, therefore selection of all variable is important for understanding mechanical results.

In addition, small changes in parameter selection can result in different times to reach equilibrium. For example, in Fig. 3, the smallest values of permeability reach equilibrium at around 60 h, while the largest value for permeability does not appear to reach a stationary value before 80 h. Therefore, choice of parameter can have a strong impact on the time it takes to reach final shrinkage

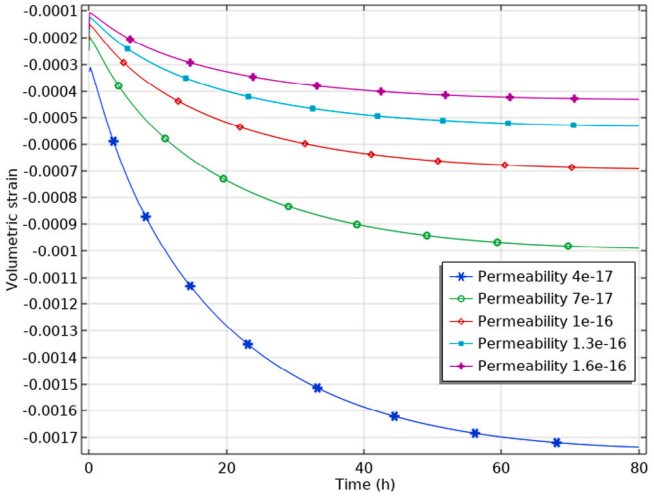

Fig. 3. Volumetric strain against time for variation of intrinsic permeability.

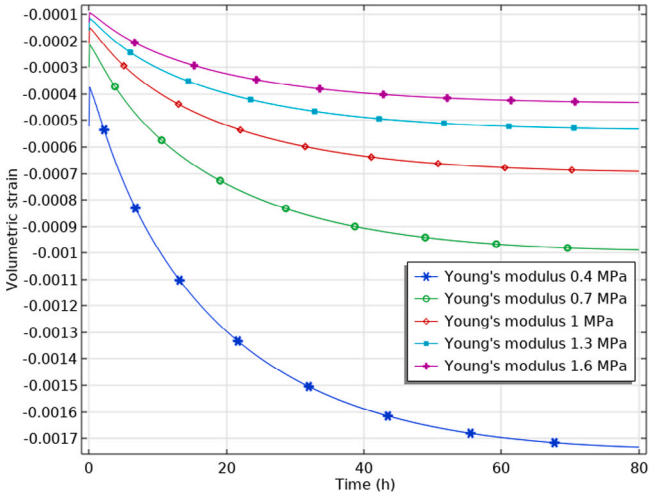

Fig. 4. Volumetric strain against time for variation of Young's modulus.

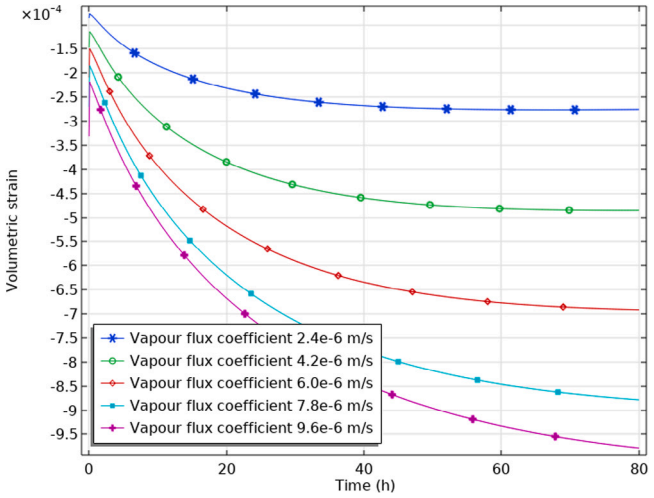

Fig. 5. Volumetric strain against time for variation of vapour flux coefficient.

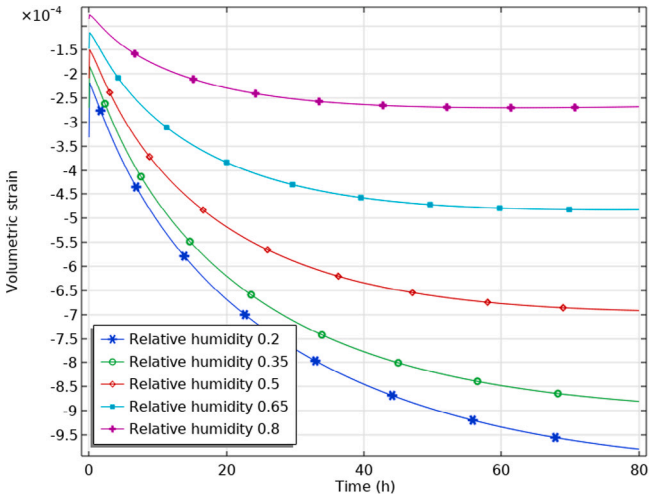

Fig. 6. Volumetric strain against time for variation of relative humidity of atmosphere.

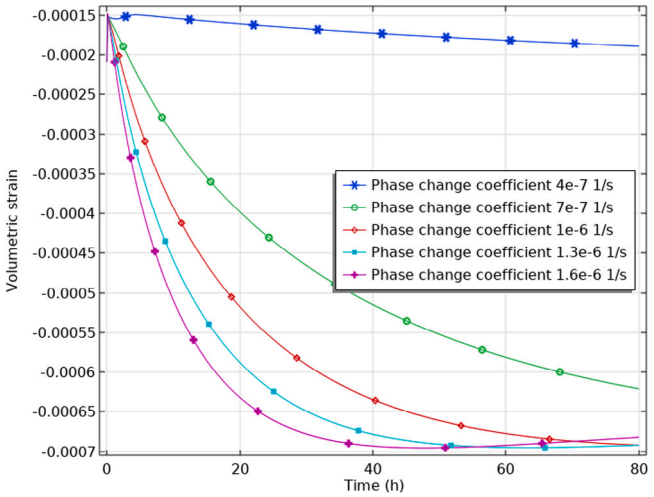

Fig. 7. Volumetric strain against time for variation of phase change coefficient.

values. We suggest this may help calibrate results when exact measurements of parameters are not known or cannot easily be measured, as it provides a feature that may be easier to compare. This can be especially important for variables such as the vapour flux coefficient and phase change coefficient that cannot be measured directly.

Another key point is that the minimum and maximum ROV for the Young's modulus are very similar, demonstrating a stable sensitivity. This reflects the results seen in other studies, in which strain and displacement do not affect the sensitivity of the Young's modulus (Abdollahipour et al., 2019; Wang et al., 2022).

5.2.2. Hydraulic changes

The ROV for the value of saturation can be found in Table 6. Only plots for variations in m_v, $(RH)_a$ and m_e have been included, in Figs. 8–10, as these were the only ones that showed visible differences between each variation.

The hydraulic properties, m_v, $(RH)_a$ and m_e, are the most sensitive parameters when it comes to saturation levels. In particular, they are on average two or three orders of magnitude more sensitive than κ and E. This highlights the importance in the selection of hydraulic properties in contrast to mechanical properties when looking at results pertaining to the presence of water in the soil.

In particular, we notice that the largest effect of parameter variation lies towards the end of the drying curve. This is likely due to the fact that the presence of water vapour in the soil is much higher than the water vapour in the atmosphere at the start, no matter the choice of parameter. Towards the end of the drying period, these values approach equilibrium, therefore the exact value of humidity and rate of vapour flux determine the amount of evaporation. Therefore, calibration of parameters is important to capture end effects of soil drying, such as the total time for the soil to dry. This was carried out in this study, taking care to calibrate parameters in order to match the total drying time to experimental results.

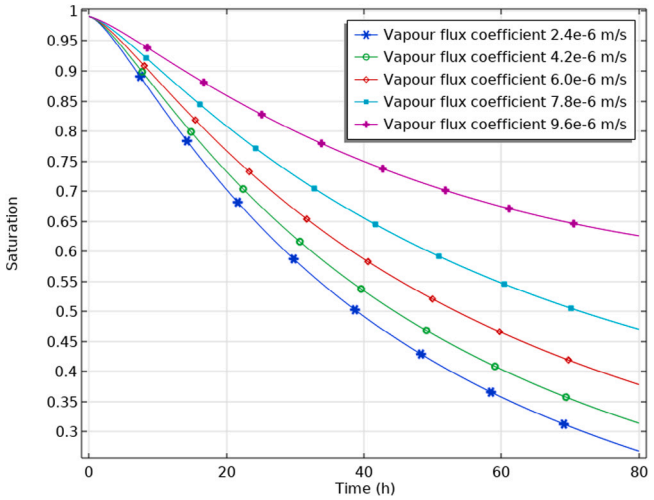

Fig. 8. Liquid saturation against time for variation of vapour flux coefficient.

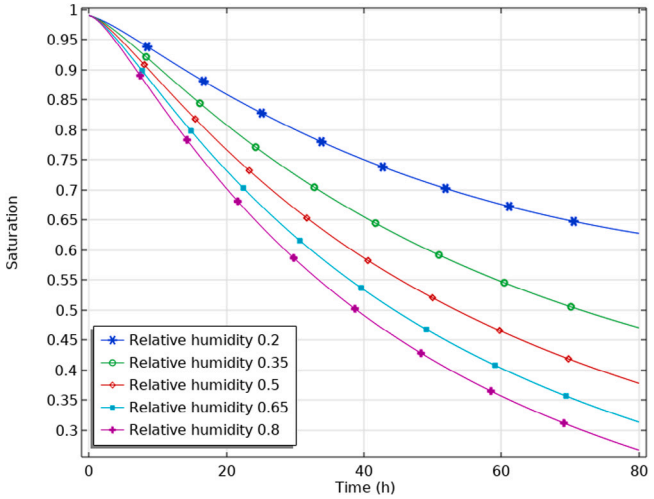

Fig. 9. Liquid saturation against time for variation of relative humidity of atmosphere.

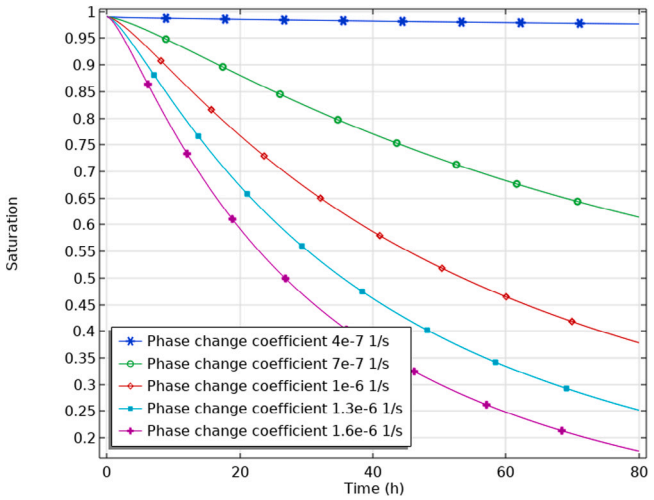

Fig. 10. Liquid saturation against time for variation of phase change coefficient.

Table 6
Calculated ROV for each parameter for saturation of liquid water.

Parameter	Variation (%)	ROV_{min}	ROV_{max}	ROV_{ave}
κ	−60	-1.82×10^{-2}	-1.89×10^{-8}	−0.00963
	−30	-9.90×10^{-3}	-3.22×10^{-8}	−0.00537
	30	8.35×10^{-8}	5.71×10^{-3}	0.00262
	60	1.16×10^{-7}	1.89×10^{-3}	0.000802
E	−60	-5.58×10^{-3}	-3.23×10^{-13}	−0.00206
	−30	-1.05×10^{-3}	-1.85×10^{-13}	−0.000389
	30	9.75×10^{-14}	5.65×10^{-4}	0.000209
	60	8.07×10^{-14}	4.586×10^{-4}	0.000169
m_v	−60	-4.87×10^{-1}	-1.13×10^{-8}	−0.260
	−30	-5.67×10^{-1}	-1.13×10^{-8}	−0.293
	30	1.13×10^{-8}	8.13×10^{-1}	0.388
	60	1.13×10^{-8}	1.09	0.484
$(RH)_a$	−60	−1.10	-1.13×10^{-8}	−0.487
	−30	-8.17×10^{-1}	-1.13×10^{-8}	−0.389
	30	1.14×10^{-8}	5.69×10^{-1}	0.294
	60	1.14×10^{-8}	4.89×10^{-1}	0.261
m_e	−60	−2.64	-4.57×10^{-7}	−1.18
	−30	−2.08	-4.57×10^{-7}	−1.03
	30	4.57×10^{-7}	1.11	0.659
	60	4.57×10^{-7}	8.94×10^{-1}	0.561

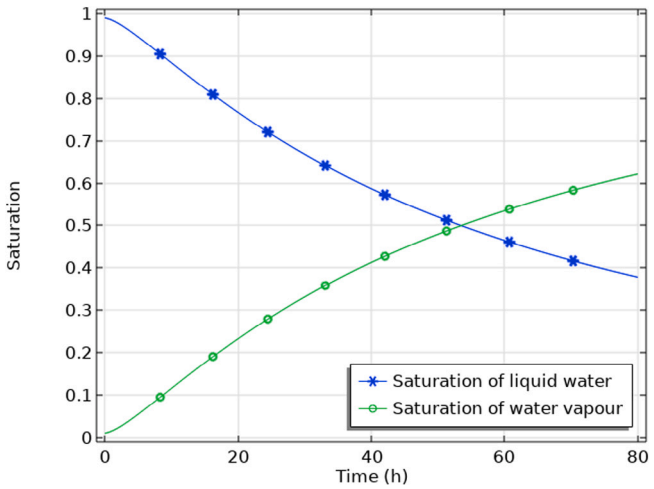

Fig. 11. Saturation of liquid water and saturation of water vapour against time for an average point.

6. Discussion and comparison of results

Select results showing the evolution of the soil and the water inside it are presented below. These demonstrate the results that can be obtained from the proposed mixture coupling theory model and highlight areas of importance.

All results shown follow the numerical implementation described in Section 3. Initial conditions and variables are set as described in Tables 1 and 2.

6.1. Evolution of properties associated with liquid water and water vapour

Fig. 11 shows the development of the soil saturation of liquid water and water vapour. The initial state starts with soil fully saturated with liquid water. As time passes, the liquid water evaporates into water vapour, causing S_l to decrease as S_v increases. This change is fairly linear, representing somewhat constant evaporation throughout the time modelled. However, the rate of change decreases slightly towards the end. We expect this to occur as the soil reaches its equilibrium dry state.

Fig. 12 shows the evolution of pressure for liquid water, water vapour, and capillary pressure. As expected during soil drying, the capillary pressure increases, while liquid water pressure decreases, representing the reduction of water of liquid form. Comparing Fig. 11 and Fig. 12, we see a similar trend in capillary pressure and saturation, as these are linked by the van Genuchten equation. However, the liquid water and water vapour pressures show different trends, with peaks at different points. This is due to differing rates of phase change and water vapour flux

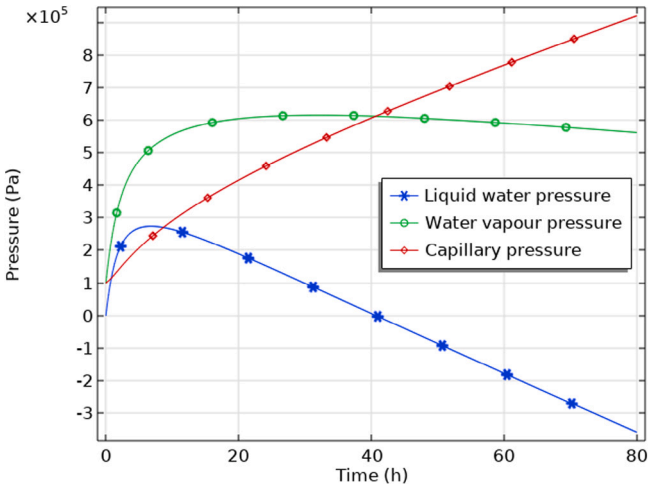

Fig. 12. Liquid water pressure, water vapour pressure, and capillary pressure against time for an average point.

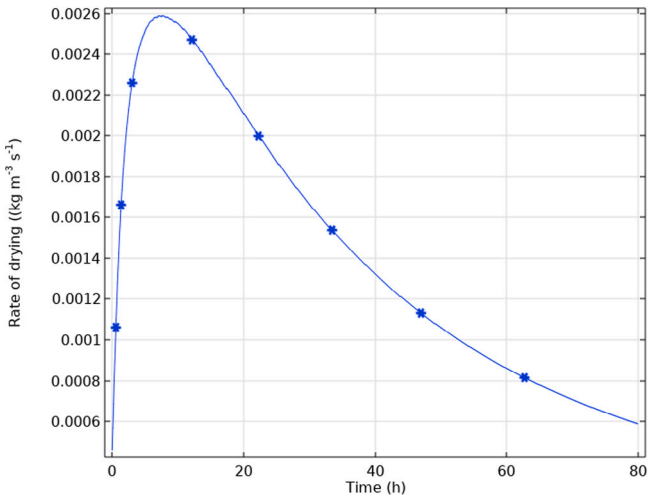

Fig. 13. Drying rate or liquid water mass change against time for an average point.

Fig. 13 shows the rate of liquid water mass change, or rate of drying. A sharp increase in drying at the start is followed by a smooth steady reduction, demonstrating that drying is focused towards the start of the process. This is representative of the experimental results given by Tamizdoust and Ghasemi-Fare (2022). The time of peak water vapour pressure in Fig. 12 falls just before the peak in drying rate: after this point, the soil experiences a much greater loss of water vapour through flux across the upper boundary.

6.2. Changes in soil structure

Fig. 14 shows the displacement of the surface of the soil over time. As expected, the soil demonstrates consolidation over time, as the water evaporates, causing the soil surface to shrink. The shrinkage tends towards a maxima, at which point the soil will not be able to shrink any further without additional forces acting up on it.

Fig. 15 shows the porosity change over time. Overall, we see the porosity decreases from 0.575 to 0.5745. Most of the porosity change occurs in the first ten hours of the drying process. This matches what was modelled by Tamizdoust and Ghasemi-Fare (2022) and found experimentally by Prime et al. (2016).

6.3. Coupling effects

Eq. (47) indicates there are three terms that affect soil porosity. To display the effect of each term, Fig. 16 demonstrates the total porosity change as well as the changes induced by each term: solid deformation, $\zeta \dot{\epsilon}_{ii}$; fluid pressure $Q\dot{\tilde{p}}$ and temperature $B_q\dot{T}$. The

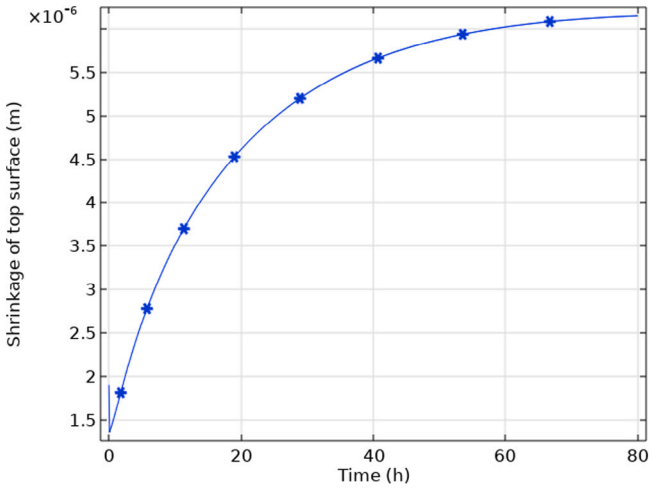

Fig. 14. Shrinkage of top surface of soil against time.

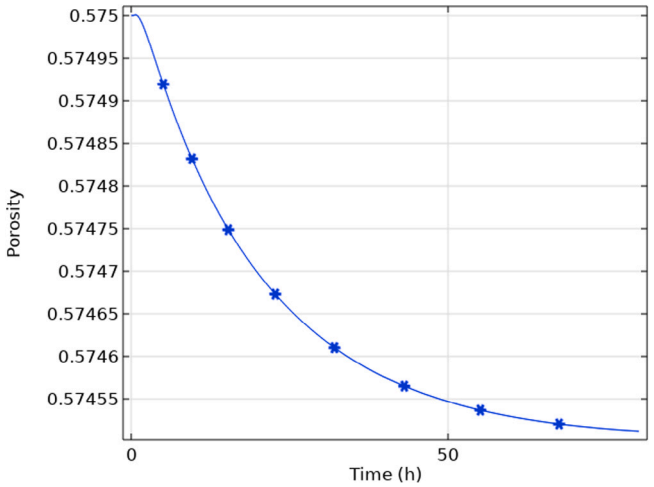

Fig. 15. Evolution of porosity against time for an average point.

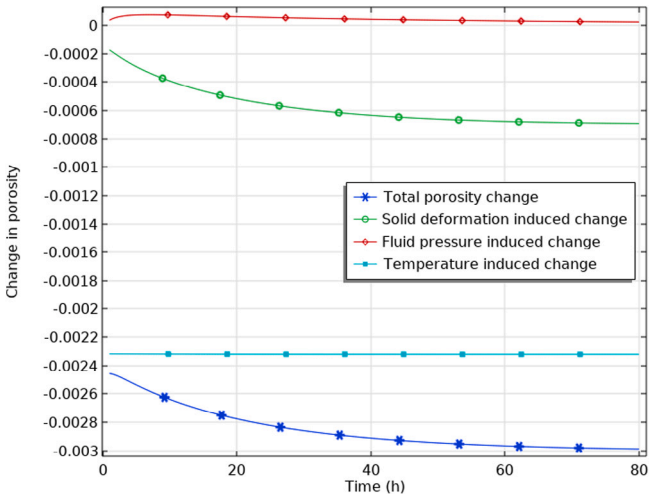

Fig. 16. Evolution of soil porosity at the central point in sample.

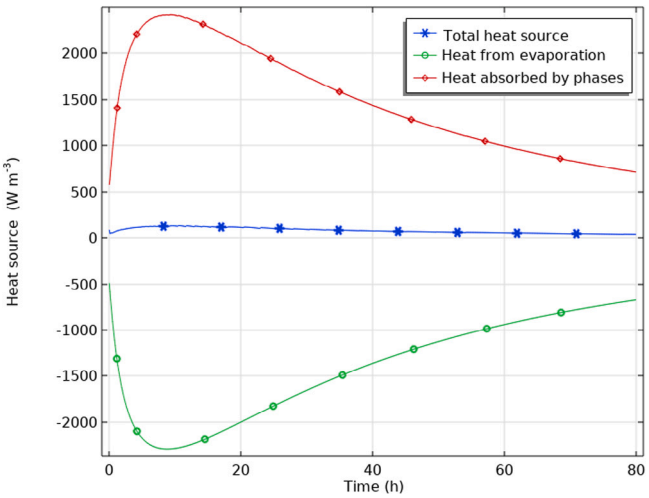

Fig. 17. Evolution of source term for temperature change.

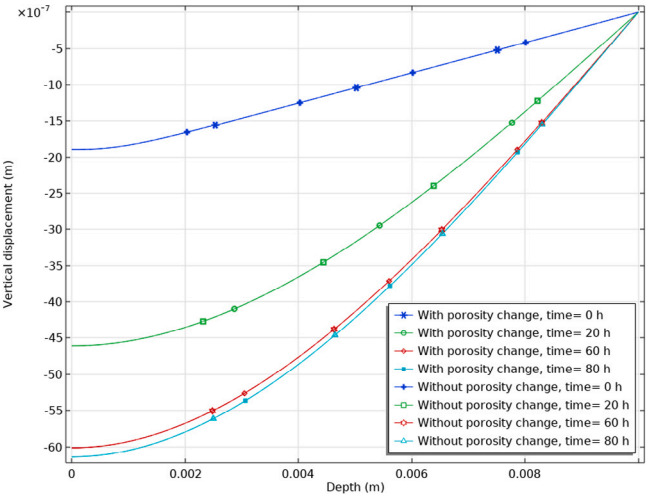

Fig. 18. Vertical displacement against depth for times$t = 0$, 20, 60, 80 h.

pressure induced change is the only positive term featured, demonstrating a constant effect of pressure against pore walls, resulting in porosity increase. Abdullah et al. (2023) suggest the pressure is highly influenced by soil properties, with higher Young's modulus resulting in smaller porosity changes, therefore we may expect the pressure impact on kaolinite to be greater than on stone or harder soils.

Both solid deformation and temperature induce porosity decrease, with temperature having the most substantial impact. As these results represent laboratory experiments, the temperature is relative unchanged throughout the drying period. However, its impact on porosity change would be more pronounced if, for example, the soil is exposed to a diurnal cycle which would result in greater variation in temperature.

To explore the impact of coupled effects on temperature change, Fig. 17 shows the total heat source broken down into heat used in evaporation and heat contained within the soil and water phases. These have opposing effects on the overall heat source, with specific heat slightly dominating, especially towards the start of the drying process.

The coupling effect of porosity change has been explored in Figs. 18 and 19, where the vertical displacement and temperature have been plotted with and without the effect of porosity change. In both cases, porosity change does not have a significant impact. However, in cases such as those with external loading as studied by Wang et al. (2022), the porosity would have a much greater effect.

The temperature at the base of the soil is lower than at the surface during the drying process, although this difference reduces over time. This can be seen due to phase change in the lower part causing heat loss, while the upper part rises in temperature as the water vapour rises into this space. Clearly, phase change is vital for the flux of temperature of soil.

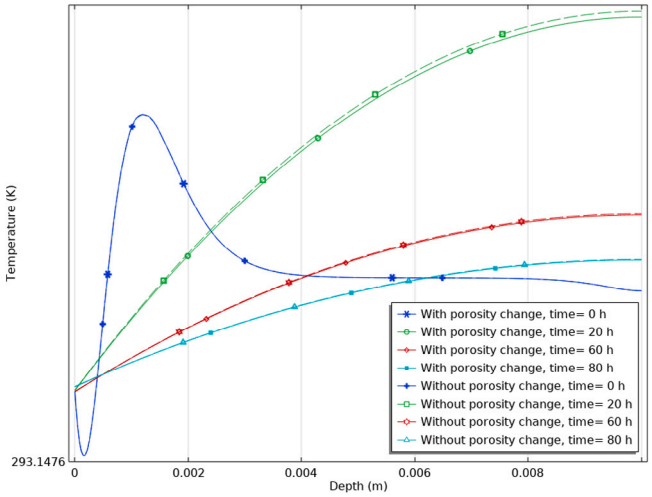

Fig. 19. Temperature against depth for times $t = 0$, 20, 60, 80 h.

7. Conclusions

In this paper, a new THM model incorporated multiphase flow and phase change based on mixture coupling theory has been presented to model soil drying. The model captures phase change from liquid water to water vapour, evaporation from the soil surface, as well as mechanical, temperature, and porosity changes in soil. The proposed model was numerically solved by COMSOL. A sensitivity analysis was conducted, highlighting the need for further experiments to identify key parameters, but key experimental trends are demonstrated to be matched by the numerical model. Then the results of multiphase flow, phase change and soil structure change were discussed using a numerical case. The model proposed shows promise for greater understanding of the underlying fully coupled behaviour during soil drying.

CRediT authorship contribution statement

Andrea Sendula: Writing – original draft, Visualization, Validation, Software, Investigation, Data curation. **Kai Wang:** Writing – review & editing, Methodology, Conceptualization. **Shashank B. Subramanyam:** Writing – review & editing, Supervision, Resources, Funding acquisition, Conceptualization. **Jake Cray:** Writing – review & editing, Visualization. **Matthew Oram:** Writing – review & editing. **Xiaohui Chen:** Supervision, Resources, Project administration, Funding acquisition. **Ana Heitor:** Funding acquisition. **David Harbottle:** Funding acquisition. **Kenny Brown:** Resources, Funding acquisition.

Declaration of competing interest

The authors declare the following financial interests/personal relationships which may be considered as potential competing interests: Shashank Bettadapura Subramanyam reports financial support was provided by European Commission Marie Sklodowska-Curie Actions. If there are other authors, they declare that they have no known competing financial interests or personal relationships that could have appeared to influence the work reported in this paper.

Data availability

No data was used for the research described in the article.

Acknowledgements

This project has received funding from the European Union's Horizon 2020 research and innovation programme under the Marie Skłodowska-Curie grant agreement No 101031565, and by EPSRC CDT in Fluid Dynamics grant number EP/S022732/1.

References

Abdollahipour, A., Soltanian, H., Pourmazaheri, Y., Kazemzadeh, E., & Fatehi-Marji, M. (2019). Sensitivity analysis of geomechanical parameters affecting a wellbore stability. *Journal of Central South University*, *26*(3), http://dx.doi.org/10.1007/s11771-019-4046-2.

Abdullah, S., Ma, Y., Chen, X., & Khan, A. (2022). A fully coupled hydro-mechanical-gas model based on mixture coupling theory. *Transport in Porous Media*, *143*(1), http://dx.doi.org/10.1007/s11242-022-01784-6.

Abdullah, S., Wang, K., Chen, X., & Khan, A. (2023). The impact of thermal transport on reactive THMC model for carbon capture and storage. *Geomechanics for Energy and the Environment*, *36*, http://dx.doi.org/10.1016/j.gete.2023.100511.

Akin, I. D., & Likos, W. J. (2020). Suction stress of clay over a wide range of saturation. *Geotechnical and Geological Engineering*, *38*(1), http://dx.doi.org/10.1007/s10706-019-01016-7.
Bai, B., Xu, T., Nie, Q., & Li, P. (2020). Temperature-driven migration of heavy metal Pb2+ along with moisture movement in unsaturated soils. *International Journal of Heat and Mass Transfer*, *153*, http://dx.doi.org/10.1016/j.ijheatmasstransfer.2020.119573.
Bai, B., Zhou, R., Cai, G., Hu, W., & Yang, G. (2021). Coupled thermo-hydro-mechanical mechanism in view of the soil particle rearrangement of granular thermodynamics. *Computers and Geotechnics*, *137*, http://dx.doi.org/10.1016/j.compgeo.2021.104272.
Bai, B., Zhou, R., Yang, G., Zou, W., & Yuan, W. (2023). The constitutive behavior and dissociation effect of hydrate-bearing sediment within a granular thermodynamic framework. *Ocean Engineering*, *268*, http://dx.doi.org/10.1016/j.oceaneng.2022.113408.
Biot, M. A. (1941). General theory of three-dimensional consolidation. *Journal of Applied Physics*, *12*(2), http://dx.doi.org/10.1063/1.1712886.
Brooks, R. H., & Corey, A. T. (1966). Properties of porous media affecting fluid flow. *Journal of the Irrigation and Drainage Division*, *92*(2), http://dx.doi.org/10.1061/jrcea4.0000425.
Brutsaert, W., & Chen, D. (1995). Desorption and the two stages of drying of natural tallgrass prairie. *Water Resources Research*, *31*(5), http://dx.doi.org/10.1029/95WR00323.
Chase, J. M. W. (1998). *Journal of Physical and Chemical Reference Data Monograph*.
Chen, X. H., & Hicks, M. A. (2013). Unsaturated hydro-mechanical-chemo coupled constitutive model with consideration of osmotic flow. *Computers and Geotechnics*, *54*, http://dx.doi.org/10.1016/j.compgeo.2013.06.001.
Chen, X., Thornton, S. F., & Pao, W. (2018). Mathematical model of coupled dual chemical osmosis based on mixture-coupling theory. *International Journal of Engineering Science*, *129*, http://dx.doi.org/10.1016/j.ijengsci.2018.04.010.
Chen, Y., Zhou, C., & Jing, L. (2009). Modeling coupled THM processes of geological porous media with multiphase flow: Theory and validation against laboratory and field scale experiments. *Computers and Geotechnics*, *36*(8), http://dx.doi.org/10.1016/j.compgeo.2009.06.001.
Cheviron, B., & Coquet, Y. (2009). Sensitivity analysis of transient-MIM hydrus-1D: Case study related to pesticide fate in soils. *Vadose Zone Journal*, *8*(4), http://dx.doi.org/10.2136/vzj2009.0023.
Dong, Y., Lu, N., & Fox, P. J. (2020). Drying-induced consolidation in soil. *Journal of Geotechnical & Geoenvironmental Engineering*, *146*(9), http://dx.doi.org/10.1061/(asce)gt.1943-5606.0002327.
Engineering ToolBox (2004). Water - Saturation Pressure vs. Temperature. In *Engineering toolBox*.
Erich, M. S., & Hoskins, B. R. (2011). Effects of soil drying on soil ph and nutrient extractability. *Communications in Soil Science and Plant Analysis*, *42*(10), http://dx.doi.org/10.1080/00103624.2011.566961.
Gardner, W. R. (1970). Field measurement of soil water Diffusivity1. *Soil Science Society of America Journal*, *34*(5), http://dx.doi.org/10.2136/sssaj1970.03615995003400050045x.
Hammouda, I., & Mihoubi, D. (2014). Thermodynamic and mechanical characterisation of kaolin clay. *Polish Journal of Chemical Technology*, *16*(1), http://dx.doi.org/10.2478/pjct-2014-0005.
Jiao, K., Lu, L., Wen, T., & Wang, Q. (2022). A modified mixture theory for one-dimensional melting of pure PCM and PCM/metal foam composite: Numerical analysis and experiment validation. *International Journal of Heat and Mass Transfer*, *186*, http://dx.doi.org/10.1016/j.ijheatmasstransfer.2021.122461.
Khalili, N., & Loret, B. (2001). An elasto-plastic model for non-isothermal analysis of flow and deformation in unsaturated porous media: Formulation. *International Journal of Solids and Structures*, *38*(46–47), http://dx.doi.org/10.1016/S0020-7683(01)00081-6.
Lekshmi, K. R. A., & Arnepalli, D. N. (2017). A review on coupled heat and water vapour transport in unsaturated soils. [ISSN: 08950563] http://dx.doi.org/10.1061/9780784480472.079.
Ma, Y., Chen, X., Hosking, L. J., Yu, H. S., & Thomas, H. R. (2022). THMC constitutive model for membrane geomaterials based on Mixture Coupling Theory. *International Journal of Engineering Science*, *171*, http://dx.doi.org/10.1016/j.ijengsci.2021.103605.
Massman, W. J. (2015). A non-equilibrium model for soil heating and moisture transport during extreme surface heating: the soil (heat–moisture–vapor) HMV-Model Version 1. *Geoscientific Model Development*, *8*(11), 3659–3680. http://dx.doi.org/10.5194/gmd-8-3659-2015.
Mcbride, B., Gordon, S., & Reno, M. (1993). *Coefficients for calculating thermodynamic and transport properties of individual species, vol. 4513: Nasa technical memorandum NASA-TM-4513*.
Miranda-Trevino, J. C., & Coles, C. A. (2003). Kaolinite properties, structure and influence of metal retention on pH. *Applied Clay Science*, *23*(1–4), http://dx.doi.org/10.1016/S0169-1317(03)00095-4.
Mondol, N. H., Jahren, J., & Bjørlykke, K. (2008). Elastic properties of clay minerals. *Leading Edge (Tulsa, OK)*, *27*(6).
Monteith, J., & Unsworth, M. (2013). *Principles of environmental physics: plants, animals, and the atmosphere* (4th ed.). http://dx.doi.org/10.1016/C2010-0-66393-0.
Pankratz, L. B. (1982). Thermodynamic properties of elements and oxides. *Bull. Us. Bur. Mines*, *672*.
Prime, N., Levasseur, S., Miny, L., Charlier, R., Léonard, A., & Collin, F. (2016). Drying-induced shrinkage of boom clay: An experimental investigation. *Canadian Geotechnical Journal*, *53*(3), http://dx.doi.org/10.1139/cgj-2015-0099.
Rajagopal, K. R. (2010). Mechanics of liquid mixtures. In *Rheology of complex fluids*. http://dx.doi.org/10.1007/978-1-4419-6494-6_3.
Rajagopal, K. R., & Saccomandi, G. (2016). A novel approach to the description of constitutive relations. In *Frontiers in materials: vol. 3*, http://dx.doi.org/10.3389/fmats.2016.00036.
Selvadurai, P., Selvadurai, P. A., & Nejati, M. (2019). A multi-phasic approach for estimating the Biot coefficient for Grimsel granite. *Solid Earth*, *10*(6), http://dx.doi.org/10.5194/se-10-2001-2019.
Simunek, J., Hendrickx, J. M. H., & Borchers, B. (2001). Modeling transient temperature distributions around landmines in homogenous bare soils. In *Detection and remediation technologies for mines and minelike targets VI: vol. 4394*, http://dx.doi.org/10.1117/12.445490.
Tamizdoust, M. M., & Ghasemi-Fare, O. (2022). Convective drying analysis of transversely isotropic natural clay. *Journal of Geotechnical & Geoenvironmental Engineering*, *148*(10), http://dx.doi.org/10.1061/(asce)gt.1943-5606.0002868.
Terzaghi, K. (1943). Theoretical Soil Mechanics. http://dx.doi.org/10.1002/9780470172766.
Truesdell, C. (1957). Sulle basi della termomeccanica. *Rendiconti Lincei*, *22*(8), 33–38.
Truesdell, C., & Toupin, R. (1960). The classical field theories. http://dx.doi.org/10.1007/978-3-642-45943-6_2.
van Genuchten, M. T. (1980). A closed-form equation for predicting the hydraulic conductivity of unsaturated soils. *Soil Science Society of America Journal*, *44*(5), http://dx.doi.org/10.2136/sssaj1980.03615995004400050002x.
Ventura, F., Faber, B. A., Bali, K. M., Snyder, R. L., Spano, D., Duce, P., & Schulbach, K. F. (2001). Model for estimating evaporation and transpiration from row crops. *Journal of Irrigation and Drainage Engineering*, *127*(6), http://dx.doi.org/10.1061/(asce)0733-9437(2001)127:6(339).
Vollet, D. R., Macedo, J. D., & Mascarenhas, Y. P. (1994). Pore structure characterization of kaolin, metakaolin, and their acid-treated products using small-angle X-ray scattering. *Applied Clay Science*, *8*(6), http://dx.doi.org/10.1016/0169-1317(94)90035-3.
Wang, K., Ma, Y., Howlett, P. R., Ding, A., & Chen, X. H. (2022). New unsaturated dynamic porosity hydromechanical coupled model and experimental validation. *International Journal of Geomechanics*, *22*(10), http://dx.doi.org/10.1061/(asce)gm.1943-5622.0002545.
Weast, C. (1998). Handbook of Chemistry and Physics-69th. *Journal of Chemical Technology & Biotechnology*, *50*(2).
Whalley, W. R., Clark, L. J., Gowing, D. J., Cope, R. E., Lodge, R. J., & Leeds-Harrison, P. B. (2006). Does soil strength play a role in wheat yield losses caused by soil drying? *Plant and Soil*, *280*(1–2), http://dx.doi.org/10.1007/s11104-005-3485-8.
Whitmore, A. P., & Whalley, W. R. (2009). Physical effects of soil drying on roots and crop growth. *60*, In *Journal of experimental botany*. (10), http://dx.doi.org/10.1093/jxb/erp200.
Zhang, Z., & Cheng, X. (2017). A fully coupled THM model based on a non-equilibrium thermodynamic approach and its application. *International Journal for Numerical and Analytical Methods in Geomechanics*, *41*(4), http://dx.doi.org/10.1002/nag.2569.